CFD modelling of natural gas combustion in IC engines under different EGR dilution and H2-doping conditions

Transportation Engineering 2 (2020) 100018

Contents lists available at ScienceDirect

Transportation Engineering

journal homepage: www.elsevier.com/locate/treng

CFD modelling of natural gas combustion in IC engines under different EGR dilution and H2-doping conditions

Mirko Baratta*, Silvestru Chiriches, Prashant Goel, Daniela Misul

Energy Department, Politecnico di Torino, Corso Duca degli Abruzzi 24, 10129 Torino, Italy

ARTICLE INFO

Keywords:
CFD
Natural gas
IC engines
Combustion modeling

ABSTRACT

The present paper provides a contribution to the CFD modelling of reacting flows in IC engines fueled with natural gas. Despite the fact that natural gas has been widely investigated into in the last decades, the literature still lacks reliable models and correlations to be exploited so as to efficiently support the design of internal combustion engines. The paper deals with the development of an accurate CFD model, capable of capturing the effects of the engine working conditions and mixture compositions on the combustion process. The CFD model is based on the Extended Coherent Flame Model combustion model coupled to a laminar flame speed one through a user subroutine, which replaces the commonly adopted empirical correlations. The flame speed values have been derived from the application of a reaction mechanism for natural gas-air-residual gases mixtures.

In the second part of the paper, the model is validated and applied to the investigation of the dependence of the combustion quality on the fuel doping with hydrogen as well as on the mixture dilution with EGR. As a matter of fact, the attractiveness of the mixture dilution with EGR relies on the potential in containing engine-out NOx emissions as well as in reducing the pumping losses, thus further abating fuel consumption at part loads. Finally, the effects of fuel blending with H2 on the EGR tolerance is discussed in the paper.

1. Introduction

In the past decades, natural gas (NG) has been used as an alternative fuel to reduce the carbon footprint of the transportation sector. NG-fuelled vehicles currently have a rather low market share, due to the limits in infrastructures. Furthermore, the intrinsic drawbacks related to cold start and low-end torque have to be considered. Such limiting factors have a tolling effect on the development of optimised gas engine technology. However, NG engine featuring technologies such as Variable Valve Actuation (VVA), Miller cycle, direct injection, lean burn mixtures, high compression ratio and boost levels, can possibly outperform gasoline or diesel engines and allow for increased thermal efficiencies and reduced pollutant emissions [1,2]. From a chemical point of view, methane is the main constituent of the NG blend and holds a large C-H bond dissociation energy [3]. More specifically, methane features a reduced laminar flame speed (LFS) and higher ignition delay time if compared to other hydrocarbons. Moreover, despite its wider lean burn range with respect to gasoline, methane does not allow for a stable homogeneous combustion beyond $\lambda \approx 1.6$ [4]. This reduces the thermal efficiency and increases the flame instability for leaner NG-air mixtures, and represents an issue for the development of lean-based innovative combustion concepts. The NG-fuelled SI engine exhibits a high cycle-to-cycle variability, thus leading to an increase of HC and CO emissions for lean-burn operations and negatively affecting the vehicle drivability. Blending natural gas with hydrogen has proven to be an effective means to overcome such limits [5,6]. Besides the possibility of extending the lean burn limit, hydrogen addition showed to exert an influence within a few percentage points on the main combustion parameters at constant ignition timing while attaining considerable HC reduction with variations in CO and CO_2 below 5% [7,8].

As it has been widely documented in the literature, the addition of hydrogen leads to an enhancement of the combustion process. As a matter of fact, the high burning speed of H_2, its higher energy content, the educed lean-burn mixture limits, the formation of a great number of H+ and OH radicals together with the higher diffusivity of the hydrogen molecules result into higher LFS of the NG-H_2 blends, as is widely documented in the literature [9–14].

Besides increasing the LFS, NG blending with hydrogen offers other advantages. The experiments conducted on a Chevrolet engine by Wallace and Catellan in [15], proved that a blend of 85% methane and 15% Hydrogen allowed for reduced brake specific fuel consumption (BSFC) and hydrocarbons (BSHC) values, still retaining increased NOx. Experiments carried out by Shudo et al. [16] proved that an increase in H_2 percentage would result into an increase in the thermal efficiency together with a decrease in the unburned HC, despite NOx increase. The achievable benefits in terms of fuel consumption were also pointed out

* Corresponding author.
E-mail address: mirko.baratta@polito.it (M. Baratta).

https://doi.org/10.1016/j.treng.2020.100018
Received 19 June 2020; Received in revised form 5 August 2020; Accepted 1 September 2020

by Bauer and Forest [17]. Moreover, the results revealed that hydrogen addition produces a decrease in the brake power up to 8% at a stoichiometric conditions and decreases in the BSFC up to 14% (for ϕ ranging from 0.58 to 1.0) if compared to the unblended NG fuelling. As far as pollutant emissions are concerned, hydrogen addition up to 60% by volume resulted in a decrease in the $BSCO_2$ up to 26% (for ϕ ranging from 0.58 to 1.0), a decrease in the BSCO up to 40% (for ϕ higher than 0.95), a decrease in the BSHC up to 60% (for ϕ ranging from 0.58 to 1.0). It is worth pointing out that the decrease in HC emissions is due not only to the reduced carbon content of the fuel, but also to a generally higher combustion efficiency as well as to a smaller quenching distance. Tunestal et al. found that hydrogen addition lowers unburned hydrocarbons emissions but increases NO_X emissions if a constant air excess ratio and ignition timing is used. The increase in the burning velocity allows the ignition timing to be retarded, thus decreasing heat losses. Higher efficiencies could hence be targeted as leaner mixture are adopted [18]. Sahoo et al. proved that the use of leaner mixtures leads to lower combustion temperatures but is likely to produce negative effects on the combustion velocity, combustion completion, IMEP and peak pressures [4]. Hydrogen addition also proved to exert positive effects on the cyclic variations of the indicated mean effective pressure (IMEP) as a consequence of the increased laminar speed [19]. The stabilising effect also increases as the mixture leans down, as pointed out by Gharehghani et al. [5].

Another advantage of H_2 addition is the extension of the flammability limits. By lowering the equivalence ratio, fuel consumption is enhanced due to reduced engine throttling for a given regime [20]. Moreover, NOx emissions can be significantly reduced if an equivalence ratio below 0.8 is operated[21]. The enhanced lean-burn characteristics of the NG-H_2 blend is a consequence of the benefits in terms of LFS. Ilbas et al. proved that increasing the hydrogen percentage in the mixture produced an increase in the burning velocity of the mixture together with a widening of the flammability limits [22]. A similar conclusion was also found in [23].

NOx emissions are effectively controlled by means of exhaust gas recirculation. EGR acts, at part load, as an additional diluent in the unburned gas mixture, thereby reducing the peak gas temperatures and therefore NOx formation rates. The effects of EGR on the engine performance and efficiency, for stoichiometric mixtures, is similar to the addition of excess air [24]. EGR also gives a few advantages, such as, the increased heat capacity with respect to the air and the possibility to run the engine under more conventional, stoichiometric, combustion modes. Substantial reductions in NOx concentrations are achieved with EGR rates ranging from 10% to 25%. On the other hand, as in the case of charge dilution with air, EGR also reduces the combustion rate, which worsens the combustion stability, and increases the HC emissions. EGR is hence to be limited up to a certain amount depending on the design of the combustion chambers, the speed and load, and the equivalence ratio [25,26]. Usually, the achievable EGR rates in SI engines range from 15% to 30%. Considering that hydrogen doping can somehow compensate the drawbacks caused by charge dilution, NG-H_2 blend fuelling combined with EGR and spark timing control is an effective approach to realise high efficiency and low-emission engines, as it was found in [27,28].

The numerical investigation and 3D model development of NG-H_2 fuelled engines has attracted great interest recently. Knop et al. [29] has worked in the improvement of the Extended Coherent Flame Model (ECFM), which was adapted to hydrogen combustion by adding a new laminar flame thickness correlation. Kosmadakis et al. [30] experimentally and numerically investigated the effect of hydrogen addition on the emission formation and has found good correlation between the two approaches. It is also worth mentioning the work of Rakopoulos et al. [31].

The present paper aims at developing and applying an accurate CFD model for the simulation of the combustion process in NG engines. As a matter of fact, the design of high efficiency SI engines featuring low CO_2 emissions requires the optimisation of quite a large number of parameters such as in-cylinder turbulence, charge dilution, fuel composition, … Given that the effects of such factors varies to a wide extent depending on the engine speed, load and combustion timing, a reliable CFD tool turns out to be of crucial importance to support the engine design and calibration phases. The paper also focuses on the model application to characterise the effects of hydrogen doping on the combustion characteristics and dilution tolerance in a small displacement engine for passenger car applications.

Table 1
Engine characteristics.

Cylinder displacement	342 cm^3
Bore/Stroke	72 mm/84 mm
Compression Ratio	9.8:1
Valves per cylinder	4
Combustion chamber	Pent-roof
Intake valve	Opening duration = 250CAD/maximum lift = 7.5 mm
Exhaust valve	Opening duration = 244 CAD/maximum lift = 7 mm
Injection system	Port Fuel injection
Turbocharger	Wastegate-controlled, fixed geometry turbine

Table 2
Fuel characteristics.

Fuel	CNG	HCNG15	HCNG25
Methane	≥98	≥83.3	≥73.5
Ethane	≤1	≤0.85	≤0.75
Butane	≤0.6	≤0.51	≤0.45
CO_2	≤1	≤0.85	≤0.85
Hydrogen avg. properties	0	15±2	25±2
α_{st}	17.05	17.40	17.70
H_f [MJ/kg]	49.1	53.7	54.6
MN	≈99	≈84	≈74

2. Methodology

2.1. Experimental dataset

The engine used for the present investigation is a turbocharged 1.4-l engine which was originally designed to run on CNG. The main specifications of the engine are listed in the Table 1. The test bench the engine was operated upon had been previously installed and instrumented. Details can be found in [23].

The engine was tested with different amounts of hydrogen added to natural gas (0%, 15%, and 25% by volume), and the engine control unit parameters were calibrated for each case to meet the hydrogen/methane blend requirements. The CNG and HCNG blends composition and main average properties are reported in Table 2:

The experimental test matrix consists in a combination of different loads (bmep=2.0–7.9 bar) and engine speeds (N=2000–4600 rpm) and the calibration was performed for MBT timing and stoichiometric steady-state conditions. Moreover, sweeps of spark timing and A/F ratio were carried out for a few selected engine working conditions. For each of the tested operation points and loads, the main engine-operating quantities (such as brake torque, crankshaft angular speed, air and fuel flow rates, and exhaust emissions) have been measured for a duration of 1 min with a sample rate of 10 Hz with controlled steady-state operation, and multiple consecutive in-cylinder pressure traces were sampled for 100 cycles according to the time base generated by the crankshaft-driven encoder (0.1 CA deg resolution). The consecutive cycles that have been measured are sufficient to provide statistical validity for the cyclic variability analysis. Each operating point has been acquired for the three considered mixtures. A selection of the available experimental dataset was considered for the calibration of the model presented in the paper.

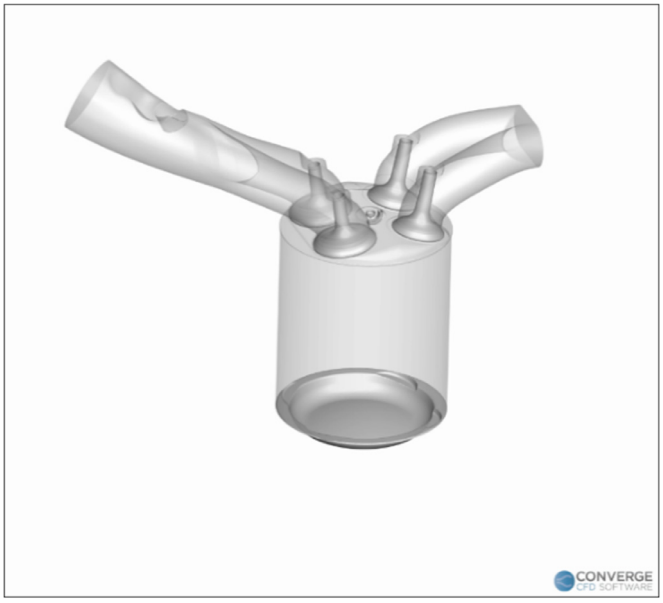

Fig. 1. CAD model of the engine combustion chamber, including intake and exhaust ports, valves and spark plug.

2.2. CFD model

The present section describes the CFD model developed within the CONVERGE software. The engine geometry is shown in Fig. 1.

Momentum and mass transport were solved for compressible flows; Redlich–Kwong equation of state was chosen to couple density, pressure and temperature. Turbulence was resolved using a Reynolds-averaged Navier–Stokes (RANS) approach with the RNG k-ε as closure model.

As far as the combustion simulation is concerned, a precise description of the detailed chemistry would be possible by embedding a detailed fuel oxidation mechanism within the SAGE module of CONVERGE to account for the species concentration. However, the main disadvantage of this method is its high computational time. Under the assumption of a perfectly uniform mixture at the intake, which is a reasonable one for a PFI engine, a good compromise between model accuracy and computational cost is achieved by using the Extended Coherent Flame Model (ECFM) coupled to the Imposed Stretch Spark Ignition Model (ISSIM) [32]. The ECFM is a flamelet-based model, which is based on the assumption that the turbulent flame is composed by a large number of flamelets, each of them behaving as a laminar flame. The ECFM represents the effect of flame wrinking by the turbulence through the introduction of a flame density per unit volume in each computational cell. The latter is calculated based on the fuel/air equivalence ratio in the unburned mixture, the composition (even if residual gases are present) and the temperature in the immediate vicinity of the flame. The resulting flame surface density is used to describe large scale burned/unburned stratification. When the spark discharge occurs, a mass of burning gases is deposited between the electrodes. The ISSIM submodel in based on the experimental observation that the initial kernel size does not depend on the mixture composition, but scales with the deposited electrical energy. ISSIM simulates the reaction rate due to the flame surface density at the ignition event. The model is capable to represent both the electric circuit energy deposition and flame surface and mass deposition, thus modelling the ignition of the first mass of unburned gases. Once the first flame kernel is formed, ISSIM takes the deformation of the gases surface due to convection and turbulence into account.

The ECFM requires the laminar flame speed to be specified as an input. In this work, in order to improve the model accuracy, a detailed model was developed based on the Aramco reaction mechanism [33] in the LOGEresearch software. The capability of the Aramco mechanism to reproduce experimental results for laminar flame speed or ignition delay was demonstrated by various researchers for single fuel feeding, for methane and hydrogen mixtures as well as for EGR diluted ones [9,34–41]. The LOGEresearch simulation results were organised in the form of a lookup table as a function of the fuel composition, EGR rate, equivalence ratio, pressure and temperature of the mixture. The lookup table was then embedded in the model by means of a user defined function. This solution represents a very good compromise between model accuracy and computational cost, with respect to the use of empirical relations [42,43] as well as to the direct mechanism implementation in the CFD code. The LFS calculation in LOGEresearch was performed for all the fuels for a wide range of pressure [1-200 bar], temperature [300-1600 K] equivalence ratio [0.1–5] and EGR [0–40 %].

Table 3
Cylinder mesh parameters during combustion.

	Base	Refined #1	Refined #2
Base grid size [mm]	4	4	3
Final size [mm]	2	1	0.375
Final size including AMR [mm]	0.25	0.25	0.375
Average Simulation Time	18 h/cycle	32 h/cycle	42 h/cycle

The LFS submodel results and validation are reported in Figs. 2 and 3. In Fig. 2, the experimental results from different researches are represented the empty red symbols whereas the numerical results are depicted by the solid black circles. The results obtained with a previous version of the submodel that embeds the GRIMECH3.0 mechanism are also reported as a reference.

The results if Fig. 2 prove that both the GRIMECH and the Aramco mechanisms are able to accurately reproduce the LFS trend versus the equivalence ratio at a pressure of 1 bar and 5 bar, respectively. However, as the pressure further increases, more accurate results were obtained with the Aramco mechanism. The accuracy of this model is further proved by Fig. 3, where the laminar flame speed versus pressure is reported for a stoichiometric mixture at two different temperatures. The symbols represent the experimental results whereas the lines were produced by the present simulation model.

2.2.1. Mesh definition

An important aspect for the 3D CFD simulation is the mesh definition. In order to assess for the mesh dependence of the simulation results, three mesh solutions were tested and are enlisted in Table 3: Base, Refined #1 and Refined #2. Each of them is characterised by a base size and is refined down to a final grid size during the simulation by either adaptive mesh refinement (AMR) or fixed embedding methods, which both apply the same scaling formula:

$$grid\ size = {}^{base\ grid}/_{2^{scale}}$$

Out of the two scaling methods, the fixed embedding is set to be activated in different regions of the CFD model as ‘permanent’ or ‘cyclic’.

The AMR is a peculiar and flexible facility embedded in the Converge software, which is useful to reduce the numerical error for variables such as velocity, temperature, turbulence or species mass fraction. The AMR algorithm will increase the refinement level (embedding) based on the estimation of the variable gradients and on the comparison to user defined thresholds. The effectiveness of the strategy is demonstrated in Fig. 4, which plots the contours of the estimated error on the velocity magnitude as superimposed to the grid aspect and velocity vectors.

The results in Fig. 6(a) have been produced by activating the AMR. Fig. 6(b) reports the results with the same mesh, without the AMR. The mesh is further refined in Fig. 6(c), still without AMR. The error is at its lowest point in Fig. 6(a), thanks to the effect of mesh refinement in the areas where the flow is under-resolved, thus reducing the error in the calculation of the velocity field. In Fig. 6(b) and(c) the error turns out to be more significant. It is worth recalling that the results presented in Fig. 6(c) were produced through a base mesh featuring half the size that

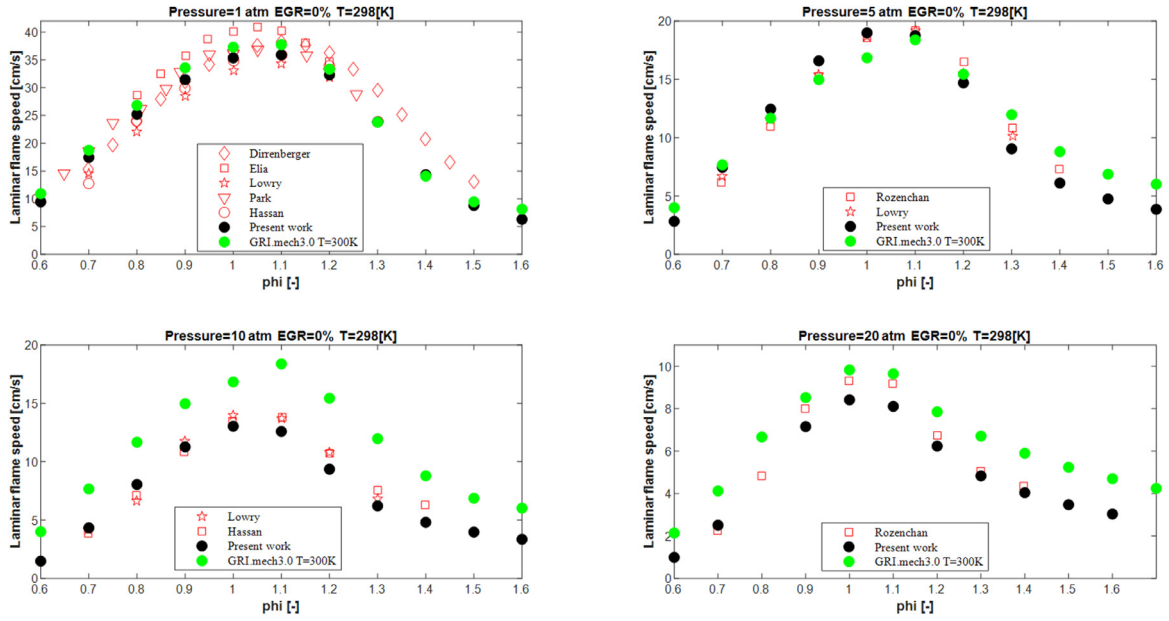

Fig. 2. Aramco Mechanism validation: LFS as a function of equivalence ratio at different pressures.

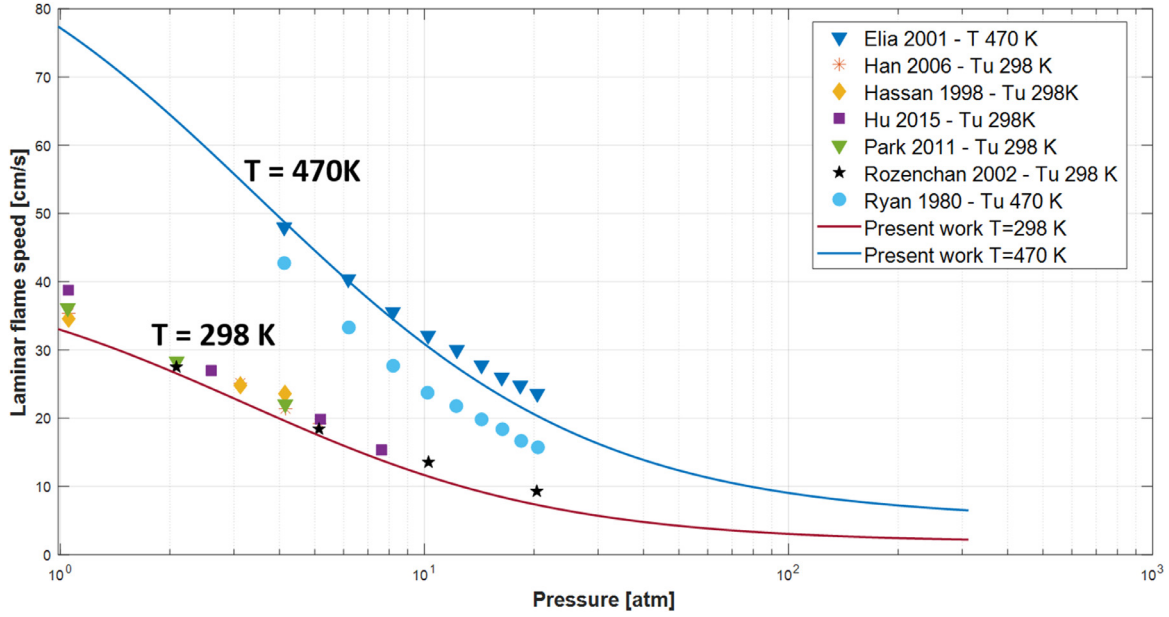

Fig. 3. Comparison of experimental laminar flame speed and present LOGEresearch model results at different pressures and temperatures, for stoichiometric mixture.

of Fig. 6(b) throughout the entire domain, thus giving rise to the highest computational time.

The results of the grid independence analysis are presented in Figs. 5 and 6 with reference to the engine working condition at 2000 rpm, 360 kPa.

As far as the ensemble-average of the simulated in-cylinder pressure in Fig. 5 is concerned, the peak firing pressure (PFP) value obtained by the Base mesh is 6% lower than that produced by Refined #2 mesh. The difference with respect to the Refined #1 mesh is 5%. This difference can be ascribed to an underestimation of the turbulence level in the Base case (about 10–15%), as well as to the spark secondary current as it is modelled by the ISSIM. The second factor holds for the Refined #2 case, where small differences can be observed, thanks to the more detailed description of the spark gap region. This impacts on the heat release calculation in the interval between the spark timing and the peak pressure occurrence. The error with respect to the Refined #2 case is of 3.5% for the trapped mass, and of around 4 deg as far as the combustion duration is concerned.

Fig. 6 shows the behaviour of the different meshes in terms of cycle-to-cycle variability. As was already documented in [44,45] in-cylinder engine simulations can show numerical cycle-to-cycle variations as the grid is refined, due to the decreased grid viscosity and, consequently, to the lack of damping effect on the initial conditions of the simulated cycles. The figure depicts the fluctuations in the ensemble average of the PFP, the fuel trapped mass and the MFB10-90 interval as the number of simulated cycles increases from 2 up to 10 (abscissa axis). More specifically, the first simulated cycle was discarded because it is affected by the initial conditions. The first point reported in Fig. 6 is the average of the considered quantity between cycle n.2 and n.3. From the second point onwards, one cycle is progressively added to the sample for the average

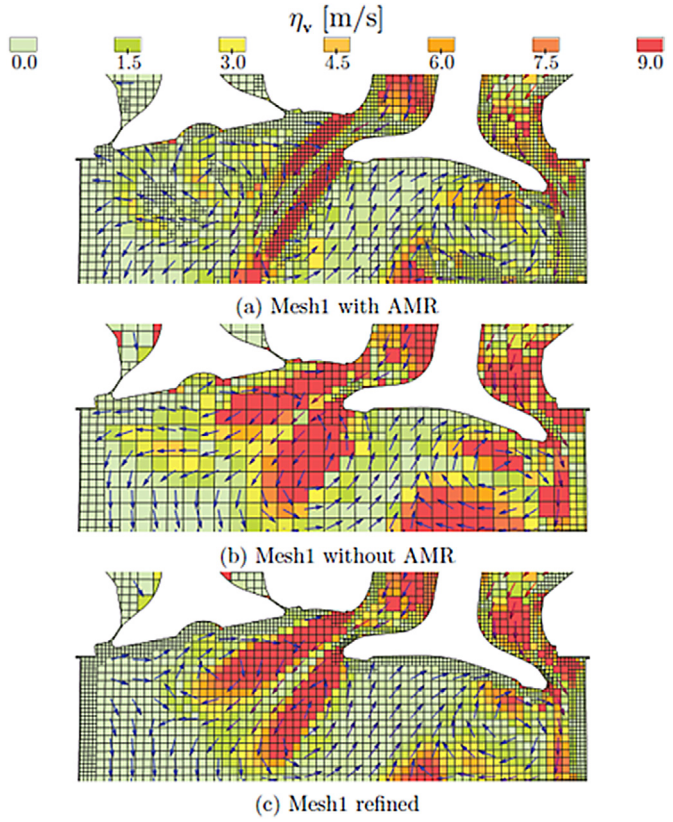

Fig. 4. Comparison between mesh, error estimator and velocity field.

evaluation. In the Base mesh case, all the reported quantities show virtually unchanged average values once the cycle n.4 is considered. This indicatesa very limited variation of the simulated quantities from one cycle to another, thus hinting at the presence of numerical viscosity capable of damping down any numerical perturbation. The refinement of the mesh leads to some difference in the averaged results, but also to a more apparent sensitivity to such perturbations.

The results obtained through the Base mesh have been considered to be the best compromise between accuracy and computational cost (see Table 3). The above mentioned differences with respect to the refined meshes can in fact be easily recovered by a slight change in the combustion model calibration constants (see next section), and do not impair

Table 4
Meshing details and scaling.

Boundary/region	Refinement type	Final size [mm]
Cylinder Region	Fixed Embedding	2
Cylinder Region	AMR	0.25
Intake region	AMR	0.25
Exhaust Region	AMR	0.5
Cylinder Head	Fixed Embedding	0.5
Cylinder Liner	Fixed Embedding	0.5
Piston Surface	Fixed Embedding	0.5
Intake Valve Top Surface	Fixed Embedding (Cyclic)	0.25
Intake Valve Bottom	Fixed Embedding	0.5
Exhaust Valve Surfaces	Fixed Embedding (Cyclic)	2
Exhaust Valve Bottom	Fixed Embedding	0.5
Spark Plug	Fixed Embedding (Cyclic)	0.125
Intake Port	Fixed Embedding	1
Exhaust Port	Fixed Embedding	2

the capability of the model to capture the effect of the main operating variables on the combustion process. It is also worth pointing out that 8 to 10 cycles would have to be simulated for the refined meshes in order to get stabilised results. Further details about the Base mesh are reported in Table 4, and a exemplification of the mesh structure during the intake stroke is provided in Fig. 7.

3. Model validation

Two operating conditions were considered for the model validation, namely, 2000 rpm x 6 bar and 3000 rpm x 8 bar, under stoichiometric conditions. Furthermore, the model was also tested for different A/F ratios at 2000 rpm x 6 bar. The following comparisons were made:

- Pressure cycles
- Combustion duration of MFB0-10; MFB 10-90
- MFB50 timing relative to TDC
- Peak Firing Pressure Crank Angle relative to TDC
- Peak Firing Pressure Value

Fig. 8 shows the comparison of the simulated and measured in-cylinder pressure traces. More specifically, different curves are presented: “Avg. Numerical Cycle” holds for the ensemble average from the 2nd to the 7th consecutive cycles from the simulations whereas “Avg. Experimental Cycle” is the ensemble average of the 100 consecutive cycles that were experimentally acquired. Each of the acquired cycles is also reported in the chart with a light grey line so as to give an insight of the cycle-to-cycle pressure fluctuations. The results of the model application to the three different engine fuelling is reported in Fig. 9, which

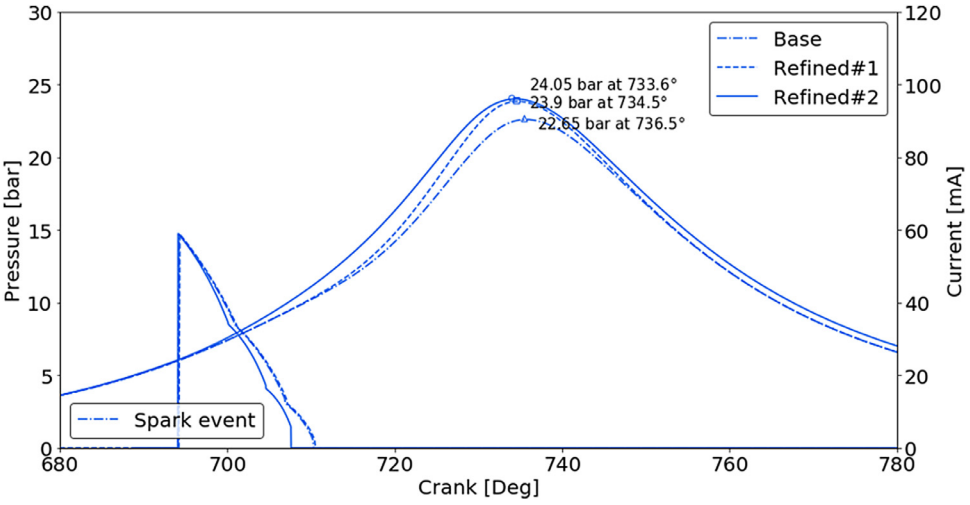

Fig. 5. Experimental pressure cycle vs numerical cycles for different mesh sizes.

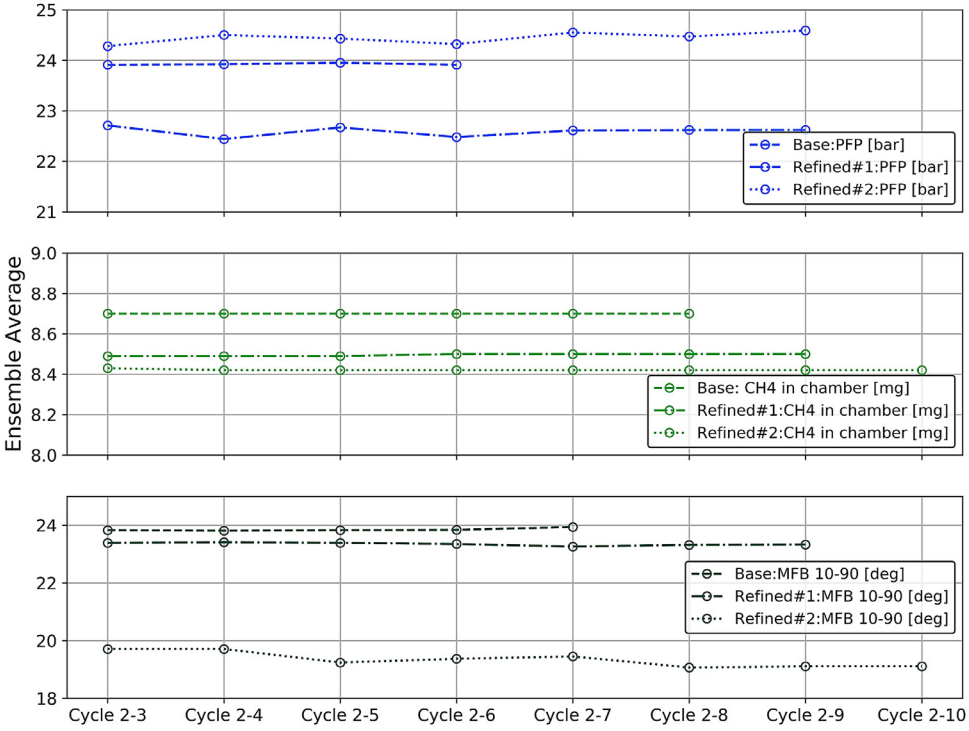

Fig. 6. Experimental vs numerical results-peak pressure, fuel trapped mass, combustion duration.

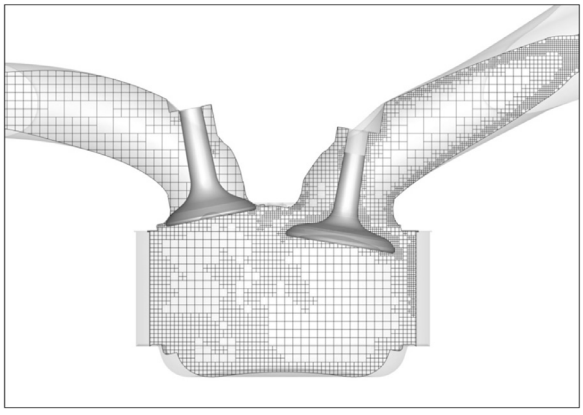

Fig. 7. Mesh details in the intake phase. AMR due to velocity gradient active at the inlet port.

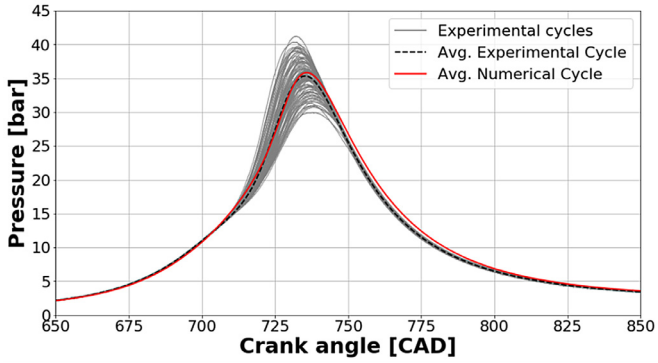

Fig. 8. 2000 × 6, lambda=1 CNG fuel.

compares the main combustion-related parameters: the black triangles refer to the experimental results whereas the red square hold for the simulations. The data are plotted against the hydrogen content of the fuel (see Table 2). The experimental values of the intake and exhaust pressure together with the temperature and with the spark timing actuated by the ECU were used as input for the simulation. The data in Figs. 9 and 10 assess for a satisfactory model accuracy. More specifically, referring to the in-cylinder pressure time history for CNG fuelling, an accurate reproduction of the experimental results stems during the compression and the combustion phases. Still, a slight overestimation of the in-cylinder pressure during expansion arises, mostly likely to be ascribed to an underestimation of the heat transfer to the cylinder walls.

The results in Fig. 9 show that the model is able to capture the effect of the fuel properties on the combustion-related parameters, without any change in the ECFM constants (flame stretch rate, wrinkling factor). More in detail, since the initial flame development angle, $\Delta\theta_{0\text{-}10}$, is marginally influenced by the in-cylinder turbulence, the good agreement in the figure is a further proof of the accuracy of the implemented LFS submodel. Furthermore, in agreement with the findings in the literature, both the CFD and the experimental results confirm the apparent increase in laminar flame speed for the hydrogen-doped fuels. A very good accuracy is also found for the $\Delta\theta_{10\text{-}90}$ combustion duration, even though the latter is less sensitive to the hydrogen content in the fuel. On the one hand, the increase in LFS due to the hydrogen doping corresponds to an increase in the turbulent burning speed [8]; on the other hand, the global effect is somehow 'filtered' by the flame-turbulence interaction. Finally, as far as the peak firing pressure and its corresponding angle are concerned, a nearly constant behaviour is observed. As a matter of fact, the differences in fuel density and flame speed were compensated by a careful control of the engine throttling and spark timing, so as to keep a constant engine load and to guarantee an optimal combustion phasing for all cases. The combustion phasing produced by the spark timing is represented by the MFB50 position in Fig. 9 and differences between 2 and 3 CA degrees can be observed. Finally, the simulated trapped mass per cycle feature an average error around 4%. However, the trend against the H2 percentage is properly reproduced for all quantities.

Further validation cases are provided in Figs. 10 and 11.

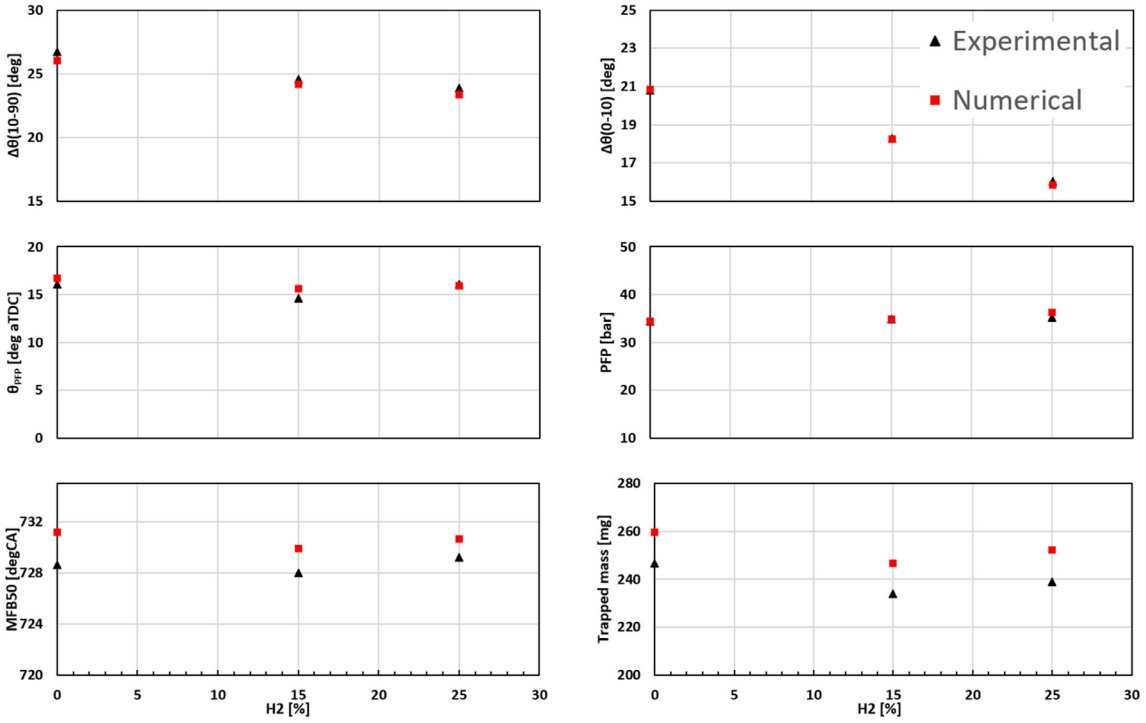

Fig. 9. 2000 rpm, imep = 6 bar, $\lambda = 1$ – Experimental and numerical combustion-related quantities and trapped mass, for different fuel compositions.

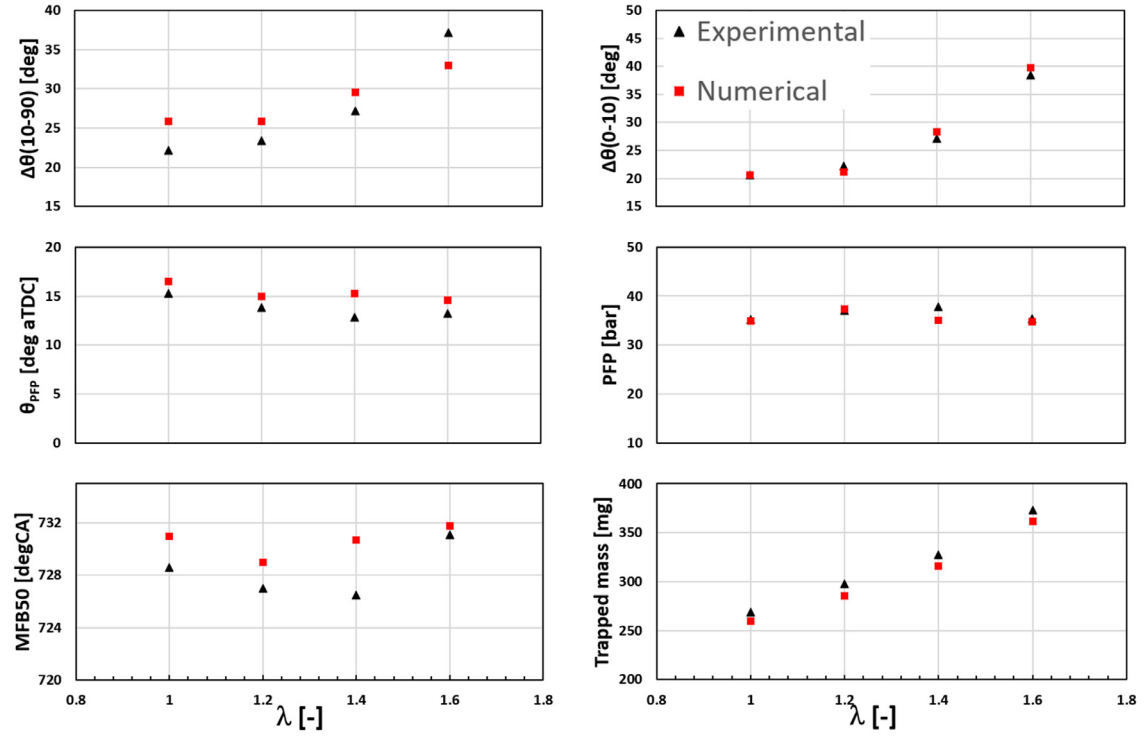

Fig. 10. 2000 rpm, imep = 6 bar – Experimental and numerical combustion-related quantities and trapped mass, for different mixture air dilution under CNG fueling.

Fig. 10 shows the comparison between experiments and CFD model for an A/F ratio sweep performed at 2000 rpm, 6 bar with CNG fuelling. The combustion development interval $\Delta\theta_{0\text{-}10}$ shows a nearly parabolic trend, which is almost perfectly captured by the model, thus further confirming the accuracy of the LFS submodel. The other combustion duration intervals are reproduced to a major extent, even though more apparent differences appear for the leaner mixtures ($\lambda = 1.4$ and 1.6).

Fig. 11 reports the results of the model validation for higher engine speed and load, for the three considered fuels, under stoichiometric conditions. Even though the trends versus H_2 percentage are less defined, the model is able to follow them, despite some more apparent differences on the $\Delta\theta_{0\text{-}10}$ interval (about 1-2 CAD) and on the MFB50 timing.

The results in the present section allow for stating that the model is able to reproduce the trends of the experimental results without

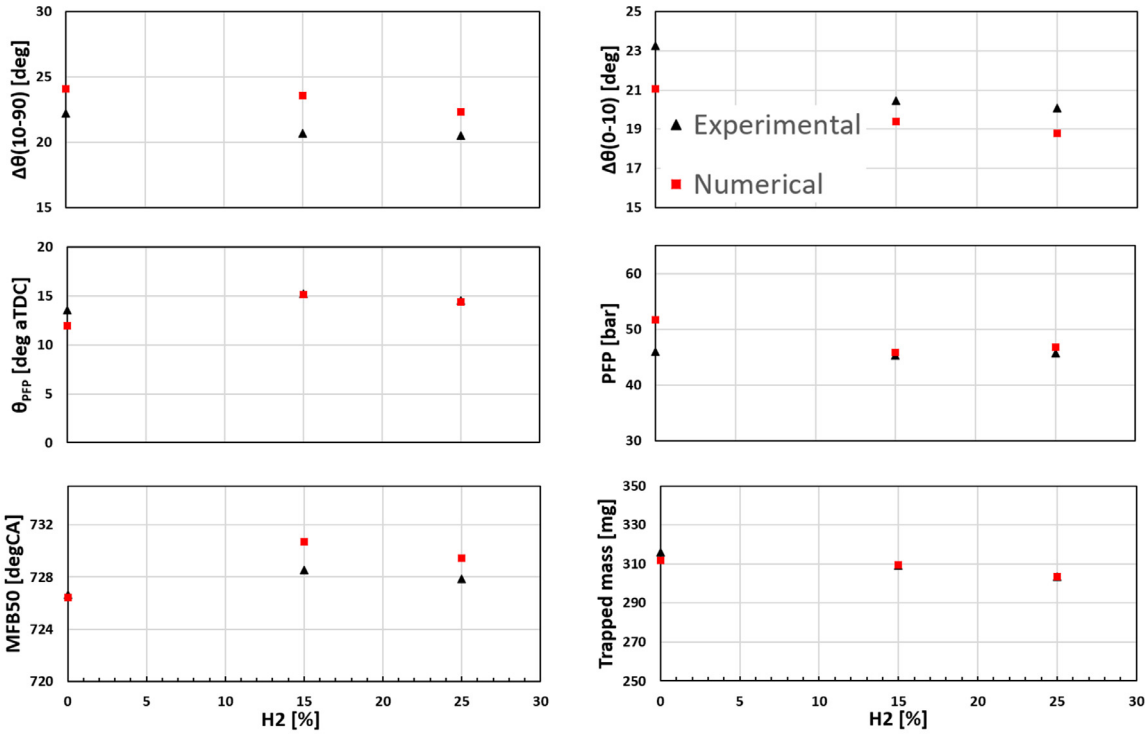

Fig. 11. 3000 rpm, imep = 8 bar – Experimental and numerical combustion-related quantities and trapped mass, for different mixture air dilution.

adjustments in the model constants. Moreover, based on the results in [44], the model, coupled with the LFS lookup tables and ECFM combustion model, is able to accurately reproduce the dependence of the combustion process on the EGR rate. This gives an additional proof of the model accuracy and indicates that it can be used as a predictive tool to investigate the combustion process in natural gas engines, with specific reference to the effects of the mixture composition.

4. Results and discussion

4.1. Borghi diagram

In this section the effects of fuel doping by hydrogen addition will be discussed in detail. Furthermore, the model will be used as a predictive tool to investigate into the effect of the charge dilution by means of exhaust gas recirculation. Both changes in the mixture composition exert a remarkable influence on the mixture laminar flame speed and, in turn, on the flame–turbulence interaction. Consequently, it is worth representing the evolution of the combustion on the well-known Borghi diagram [46]. This chart represents the state of a homogeneous burning mixture by referring to the following non-dimensional numbers:

4- the ratio between the integral length scale of the turbulence (L_t) and the flame thickness (δ_F);
4- the ratio between the turbulence intensity (u') and the laminar flame speed (S_L).

The turbulence integral length scale is calculated as:

$$L_t = \left(\frac{u'^3}{\varepsilon}\right) \tag{1}$$

where $u' = \sqrt{\frac{2}{3}k}$ is the turbulent velocity fluctuation, which is derived from the turbulent kinetic energy. The latter is in turn calculated using the transport equation in the k-ε closure model [47]. The flame thickness is defined as

$$\delta_F = \frac{\left(\lambda/c_p\right)_0}{\left(\rho S_L\right)_u} \tag{2}$$

where the heat conductivity λ and the heat capacity, c_p are evaluated at the inner flame temperature T_0, whereas the denominator is evaluated with reference to the in the unburned gas [48]. In the context of the CFD model, δ_F is calculated as described in [49].

As the abovementioned quantities are not homogeneous in the combustion chamber, volume-averaged values are evaluated by the software, through a purposely defined user subroutine. In the Borghi chart several combustion regimes can be defined, based on the range of the Karlovitz number, $Ka = \tau_c/\tau_k$. The latter is the ratio between a time scale representative of the chemical reactions and a time scale of the turbulence field [46], given by:

$$\tau_c = \frac{\delta_F}{S_L} \tag{3}$$

$$\tau_k = \frac{L_t}{u'} \tag{4}$$

l_k and u_k, in turn, are the characteristic size and velocity for the turbulent structures at the Kolmogorov scale level. As the latter are difficult to be evaluated from a RANS simulation, following the indication in [46], the Karlovitz number is finally evaluated as:

$$Ka = \left(\frac{u'}{S_L}\right)^{3/2}\left(\frac{L_t}{\delta_F}\right)^{-1/2} \tag{5}$$

4.1.1. Hydrogen addition effects

Fig. 12 shows the evolution of the combustion process for the engine working point at 2000 rpm, bmep = 6 bar, λ = 1, for the three fuel compositions (see Table 2). The objective is to support the interpretation of the results already showed in Section 3, so as to gain fundamental knowledge on the combustion process for the considered fuels.

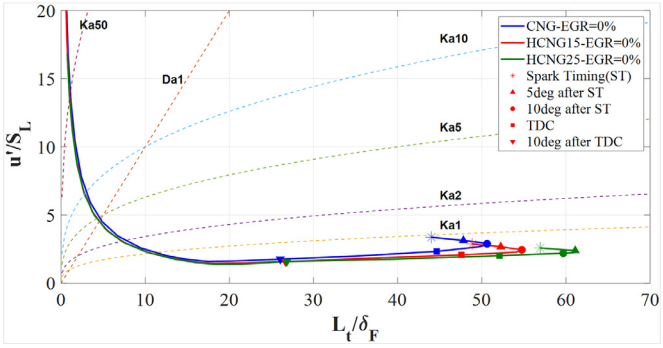

Fig. 12. Trend of the combustion curves for the three fuels- CNG, HCNG15 and HCNG25, EGR0 %.

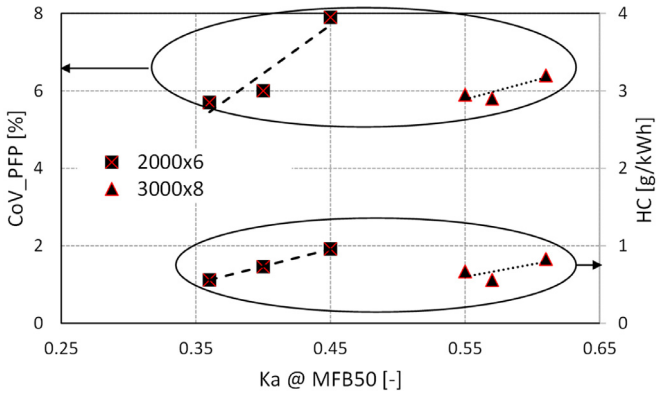

Fig. 13. Relation between Karlovitz number, CoV_PFP and HC formation with hydrogen addition.

The results are presented in Fig. 12. The different colours denote the three fuel compositions. The curves were plotted from spark timing (ST) to the exhaust valve opening, and a few relevant crank angle positions were highlighted with symbols on each curve, as indicated by the legend. It is worth mentioning that the ST was set in such a way to reach MBT (maximum brake torque), by targeting a MFB50 timing in the range from 7 to 10 deg after TDC. As the fuel composition is changed by adding hydrogen to the blend, the portion of the curves from the spark advance till a few degrees after TDC are shifted towards the bottom-right corner. The vertical translation can be justified by taking into account the combination of two effects:

- different thermodynamic conditions (higher pressure and temperature for the hydrogen-blended fuels) due to lower spark timing, thus leading to a higher laminar flame speed;
- the decrease in turbulent intensity (u') determined by the earlier crank angle for the CNG case and, consequently, by the lower turbulence decay.

Although the sensitivity of the combustion pattern on the hydrogen dilution is rather limited in the case of Fig. 12, the figure is useful to exemplify that the combustion quality can somehow be diagnosed on the Borghi diagram. More precisely, a shift of the combustion-evolution pattern towards the bottom-right corner corresponds to a decrease in the average Karlovitz number. It can be seen that the Karlovitz number in correspondence of the MFB50 timing correlates well to some experimental combustion-related measurements. In particular, Fig. 13 shows the correlation with the experimental cylinder-averaged CoV of the peak firing pressure (left axis) and brake specific HC emissions (right axis). The experimental results have been previously published in [21,23]. As the Karlovitz number at the MFB50 crank angle decreases, the coefficient of variation of the peak firing pressure decreases, hinting at a

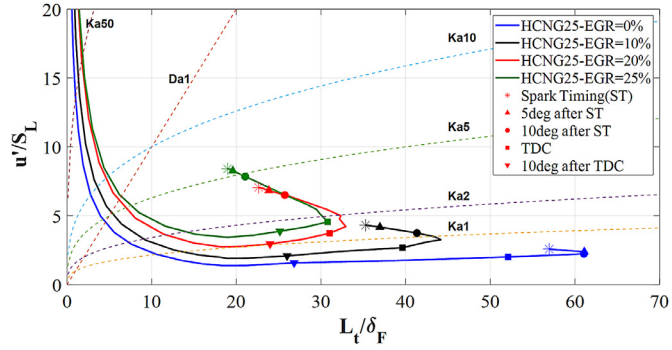

Fig. 14. HCNG25 fueling- EGR sweep.

reduced cycle-by-cycle variability of the combustion process. Similarly, it can be deduced that an increase in Ka at MFB50 leads to an increase in the sensitivity of the combustion on the cycle-by-cycle perturbations of the turbulent flow. The decrease in the HC emission as Ka decreases is also due to the reduced combustion variability, as less cycles featuring a low combustion efficiency occur. It is anyway worth pointing out that all the combustion events are confined to the diagram region with Ka<1 ('flamelet regime'), which is characterised by a good stability of the combustion process, being the experimental CoV of the engine imep below 1% [21].

4.1.2. EGR dilution

As it was mentioned in the introduction, hydrogen addition to natural gas can increase the EGR tolerance of a given engine, leading to advantages in terms of both fuel consumptions and NOx emissions. The benefits are in fact a combination of the increased combustion stability (due to the hydrogen addition) and the reduced burned-gas temperature (due to the dilution with EGR) [50]. As the benefits depend on the percentage of hydrogen fraction and EGR, it is important to find out which combination of EGR and hydrogen provides the best results in terms of combustion stability for each of the tested fuel. The CFD model presented in this paper can be of great help in such an analysis. As an application, it has been used to find the maximum amount of EGR tolerated by the engine under study (Table 1), while maintaining a stable combustion. The simulations were run by adjusting the spark timing so as to keep the MFB50 position nearly constant, and by controlling the boost level to guarantee a constant engine imep. According to the findings in [51] the EGR limit was detected based on the attainment of a limit value of around 50 deg for the MFB0-50 interval. However, a significant support to such analysis could be obtained from the analysis of the combustion patterns on the Borghi plot, as a corresponding threshold value for the Karlovitz number can also be detected.

In order to analyse the effect of EGR on the combustion, the case of 2000 rpm, 6 bar, HCNG25 fuelling was initially considered and is hereafter presented. The results for the CNG and HCNG15 will also be discussed.

Fig. 14 shows the corresponding Borghi plot for HCNG25. The different EGR values are represented by the different colours as indicated in the legend, whereas the symbols retain the same meaning as in Fig. 12.

Without external EGR (blue curve) the value of Karlovitz number keeps lower than unity for most of the combustion process. As the mixture is diluted with EGR, the curves moves towards the top-left corner, leading to overall increases in the Karlovitz number. As a matter of fact, the combustion is affected by the presence of the inert gas. With the lowest EGR contribution (EGR10% - black curve), the ratio of L_t/δ_f on the x-axis decreases to a great extent for the initial combustion phase (from ST to TDC). By further increasing the EGR quantity, the ratio further increases (red and green curve), indicating that the flame thickness is heavily affected by the EGR dilution. In fact, the turbulent length scale L_t depends on the fluid motion inside the cylinder and has a limited de-

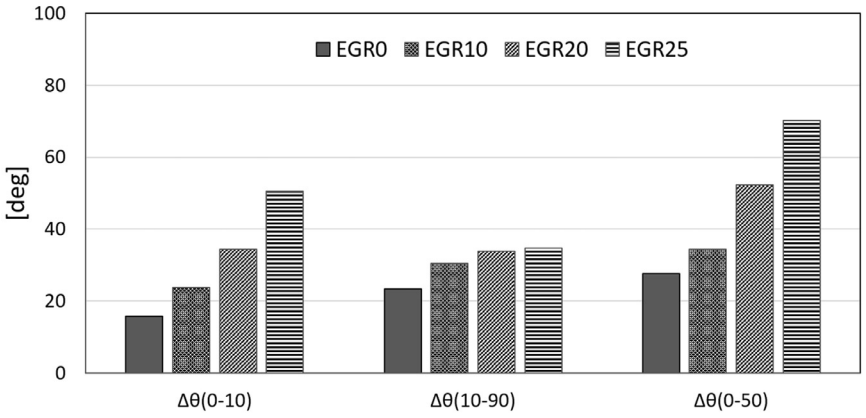

Fig. 15. Combustion intervals for different EGR rates – HCNG25 fueling, 2000 rpm, imep = 6 bar, $\lambda = 1$.

pendence on the EGR rate, for a given engine speed and load. At the same time, the flame thickness decreases as EGR increases. This can be explained by observing that Eq. (2) can be rewritten as

$$\delta_F = \frac{D}{S_L} \tag{6}$$

which shows a dependence of the flame thickness on thermal diffusivity, D, and laminar flame speed. An increase in the EGR rate produces a decrease in D as it was found in [52] The combined effect of the thermal diffusivity and the laminar flame speed produces a decrease in δ_F as is also documented by the experimental findings in [53,54].

The velocity ratio $^{u'}/_{S_L}$ is also heavily dependent on the EGR quantity. This is mainly an effect of the decrease in S_L due to the dilution effect, as well as to the increase in u' determined by the more advanced combustion timing. Consequently, the relative strength between turbulence and combusiton is modified and the combustion regime gradually moves towards the distributed reaction or pocket flame region [46].

Fig. 15 shows the dependence of the combustion duration intervals on the EGR rate.

The effect of the EGR dilution on the combustion duration are opposite to those observed in the case of hydrogen blending (Figs. 9 and 11). As the EGR increases, the flame development interval, $\Delta\theta_{0\text{-}10}$, increases, due to the reduction of the laminar flame speed in the diluted mixture. A roughly corresponding increase is visible in the $\Delta\theta_{0\text{-}50}$ interval. Consequently, the ST needs to be correspondingly increased to keep a nearly constant absolute MFB50 timing. On the other hand, the combustion duration shows an apparently lower dependence on the EGR content, in analogy to what observed in Figs. 9 and 11.

As far as the engine performance are concerned, as long as the combustion process remains sufficiently stable, the penalty in the imep induced by the charge dilution can be recovered by an increase in the boost pressure, as already observed in [51]. Also, for a given boost pressure, an increase in the spark advance can help in restoring the target imep value. As EGR is gradually increased, a threshold is reached, beyond which the combustion process quickly switches to an incomplete one. At the same time, a boost increase becomes ineffective to recover the original engine imep. As an example, Fig. 16 reports the methane concentration, indicating the progress of the combustion, at the crank angle position corresponding to the optimal MFB50 position. The left image is relative to the case with EGR=0 and shows a regular and compact flame front. The image on the right (EGR=25%) shows that the combustion progress is retarded, even if the spark advance was increased up to the unfeasible limit of 59 deg CA. A largely incomplete combustion is hence obtained. Furthermore, the shape of the flame front reveals a broken structure, which is consistent with the Ka range assumed by the combustion curve on the Borghi plot (see Fig. 14), which falls in the distributed reaction zone. In fact, when Ka>1, the turbulent flow is able to affect and to thicken the flame preheat zone by extracting heat

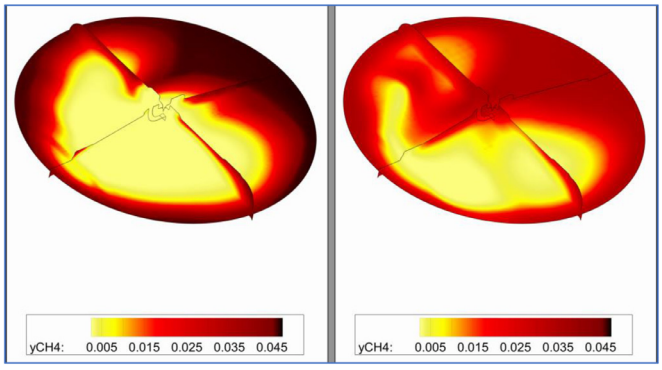

Fig. 16. Methane concentration contours at TDC+10 CAD with HCNG25 fueling: EGR = 0 (left) and EGR = 25% (right).

Table 5
EGR limit for the three fuels – 2000 rpm, imep = 6 bar.

FUEL	EGR %	$imep_{actual}/imep_{target}$ [-]	$MFB_{0\text{-}50}$ [CAD]	Ka@MFB50
CNG	10	0.98	49	0.84
HCNG15	15	1.00	48	0.90
HCNG25	20	0.95	54	1.14

Table 6
EGR rate beyond the limit for the three fuels – 2000 rpm, imep = 6 bar.

FUEL	EGR %	$imep_{actual}/imep_{target}$ [-]	$MFB_{0\text{-}50}$ [CAD]	Ka@MFB50
CNG	15	0.88	51.5	0.93
HCNG15	20	0.87	56	1.14
HCNG25	25	0.82	70	1.56

from the reaction zone, thus slowing down the combustion and, in some cases, breaking the flame front [46].

Finally, in accordance to the findings in [51], the EGR limit concentration could be detected as the one producing the achievement of the MFB0-50 combustion interval beyond 50 CAD. For the HCNG25 fuel, this corresponded to the 20% in mass. When the concentration increased to 25% (green curve in Fig. 14), the MFB0-50 interval further increased and a largely incomplete combustion was obtained. Furthermore, it was not possible to restore the target imep value, regardless of the imposed boost pressure.

Similar results were obtained by performing an EGR sweep with CNG and HCNG15. Table 5 and 6 summarises the result obtained with reference to a concentration equal to and just beyond the tolerance limit, respectively. The corresponding curves representation on the Borghi chart are depicted in Figs. 17 and 18.

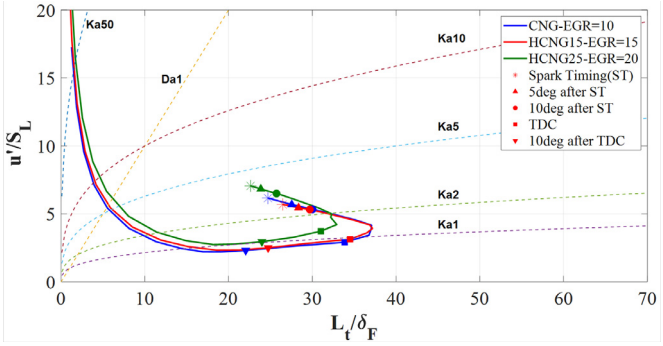

Fig. 17. Borghi Diagram for the limit EGR rate for the three fuels – 2000 rpm, imep = 6 bar.

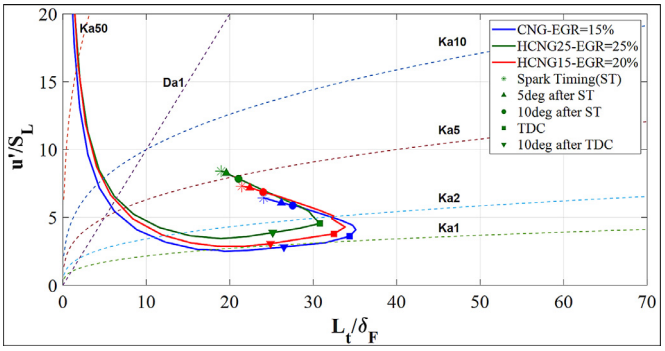

Fig. 18. Borghi Diagram for the EGR rate beyond the limit for the three fuels – 2000 rpm, imep = 6 bar.

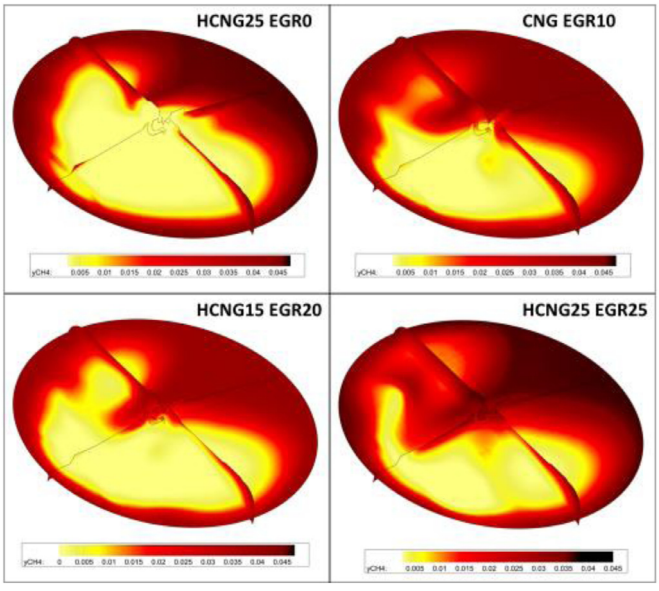

Fig. 19. Methane concentration contours at TDC+10 CAD for stable (top left), nearly unstable (top right, bottom left) and ustable (bottom right) combustion.

As expected, all the combustion curves are placed in the zone between Ka = 1 and Ka = 2. A Karlovitz number around unity at MFB50 timing can be assumed as representative for the limit dilution conditions in the considered engine. Significant detriment in the combustion stability and completeness are obtained when Ka is in the range between 1 and 1.4. The outcomes of the Borghi plot are consistent with the representation of the flame in Fig. 19. More precisely, as the Karlovitz number gets beyond the unity, the flame front is broken.

Finally, Fig. 19 also confirms the hypothesis of the Borghi Diagram (Combustion curves above Ka=1); more precisely it shows that the flame front has been broken in the cases of incomplete combustion.

5. Conclusion

In this paper the development of a CFD model for the turbulence and combustion simulation in spark ignited NG engines was presented. The model features an accurate submodel for the evaluation of the laminar flame speed for different fuel compositions and mixture dilution, which replaces the more common application of empirical correlations. The flame speed values have been derived from the application of a reaction mechanism for natural gas-air-residual gases mixtures, in which both the thermodynamics conditions, the fuel-to-air ratio and the exhaust gases concentration have been varied over a wide range.

The presented model was then validated and applied to the investigation of the dependence of the combustion quality on the fuel doping with hydrogen and on the mixture dilution with EGR. As a matter of fact, the attractiveness of mixture dilution with EGR is due to the potential in the reduction of the pumping losses, thus reducing the fuel consumption at partial load, as well as to the control of engine-out NOx emissions. The effect of fuel blending with H2 on the EGR tolerance was discussed in the paper.

The effect of fuel doping with hydrogen can be summarised as follows:

- The mixture laminar flame speed increases, and the spark advance needs to be reduced to keep the optimal combustion phasing.
- The effect on the turbulent combustion duration is less apparent.
- The comparison of the combustion patterns on the Borghi plots shows that an overall decrease in the combustion Karlovitz number is obtained as hydrogen is added to the fuel. The combustion stability correspondingly increases and the HC emissions decrease.

The extension of the analysis by including charge dilution with EGR has shown that hydrogen doping can increase the EGR tolerance of the engine, in agreement with the findings with the literature. In this paper, the analysis was based on the combined study of the engine-related variables and of the combustion evolution on the Borghi plot. It was thus possible to detect a threshold of the Karlovitz number, which corresponds to a combustion stability limit. A Karlowitz number around unity at MFB50 timing can be assumed as representative for the limit dilution conditions in the considered engine. Significant detriment in the combustion stability and completeness are obtained when Ka is in the range between 1 and 1.4.

Declaration of Competing Interest

The authors declare that they have no known competing financial interests or personal relationships that could have appeared to influence the work reported in this paper.

Acknowledgements

Tha authors would like to acknowledge the support of Rainer Rothbauer, Jyothish Venkataramanan and Pietro Scienza (Convergent Science) for their valuable suggestions, as well as for their support in the development of the user defined function embedded in the model. Convergent Science and LOGEsoft are also acknowledged for providing academic licenses for the CONVERGE and LOGEresearch softwares.

References

[1] B. Douailler, F. Ravet, V. Delpech, D. Soleri, B. Reveille, R. Kumar, Direct injection of CNG on high compression ratio spark ignition engine: numerical and experimental investigation, in: Proceedings of SAE 2011 World Congress & Exhibition, XX, 2011, pp. 1–13.

[2] M. Baratta, et al., Development of a high performance natural gas engine with direct gas injection and variable valve actuation, SAE Int. J. Engines 10 (5) (2017) 2535–2551.
[3] Y.-R. Luo, Handbook of Bond Dissociation Energies in Organic Compounds, 1st ed., CRC Press, Boca Raton, 2002.
[4] S. Sahoo, S. Tripathy, D.K. Srivastava, Performance and combustion investigation of a lean burn natural gas engine using CFD, in: Proceedings of ASME 2018 Internal Combustion Engine Division Fall Technical Conference, ICEF, 1, 2018, pp. 1–9. 2018.
[5] A. Gharehghani, R. Hosseini, M. Mirsalim, T.F. Yusaf, A computational study of operating range extension in a natural gas SI engine with the use of hydrogen, Int. J. Hydrogen Energy 40 (17) (2015) 5966–5975.
[6] S.O. Akansu, Z. Dulger, N. Kahraman, T.N. Veziroğlu, Internal combustion engines fueled by natural gas - Hydrogen mixtures, Int. J. Hydrogen Energy 29 (14) (2004) 1527–1539.
[7] A. Mariani, M.V. Prati, A. Unich, B. Morrone, Combustion analysis of a spark ignition i. c. engine fuelled alternatively with natural gas and hydrogen-natural gas blends, Int. J. Hydrogen Energy 38 (3) (2013) 1616–1623.
[8] M. Baratta, D. Misul, Development of a method for the estimation of the behavior of a CNG engine over the NEDC cycle and its application to quantify for the effect of hydrogen addition to methane operations, Fuel 140 (2015) 237–249.
[9] E. Hu, et al., Laminar flame speeds and ignition delay times of methane-air mixtures at elevated temperatures and pressures, Fuel 158 (2015) 1–10.
[10] Z. Huang, Y. Zhang, K. Zeng, B. Liu, Q. Wang, D. Jiang, Measurements of laminar burning velocities for natural gas-hydrogen-air mixtures, Combust. Flame 146 (1–2) (2006) 302–311.
[11] M. Brower, et al., Ignition delay time and laminar flame speed calculations for natural gas/hydrogen blends at elevated pressures, in: Proceedings of ASME Turbo Expo, 2, 2012, pp. 1005–1016.
[12] E.C. Okafor, A. Hayakawa, Y. Nagano, T. Kitagawa, Effects of hydrogen concentration on premixed laminar flames of hydrogen-methane-air, Int. J. Hydrogen Energy 39 (5) (2014) 2409–2417.
[13] V. Di Sarli, A. Di Benedetto, Laminar burning velocity of hydrogen-methane/air premixed flames, Int. J. Hydrogen Energy 32 (5) (2007) 637–646.
[14] P. Dagaut, G. Dayma, Hydrogen-enriched natural gas blend oxidation under high--pressure conditions: experimental and detailed chemical kinetic modeling, Int. J. Hydrogen Energy 31 (4) (2006) 505–515.
[15] J. Wallace, A. Cattelan, Hythane and CNG fuelled engine exhaust emission comparison, Hydrogen Energy Prog. 3 (1994) 1761.
[16] T. Shudo, K. Shimamura, Y. Nakajima, Combustion and emissions in a methane DI stratified charge engine with hydrogen pre-mixing, JSAE Rev. 21 (1) (2000) 3–7.
[17] C.G. Bauer, T.W. Forest, Effect of hydrogen addition on the performance of methane–fueled vehicles. Part I: effect on S.I. engine performance, Int. J. Hydrogen Energy 26 (1) (2001) 55–70.
[18] P. Tunestål, M. Christensen, P. Einewall, T. Andersson, and B. Johansson, "SAE Technical Hydrogen Addition For Improved Lean Burn Capability of Slow and Fast Burning Natural Gas Combustion Chambers," vol. 2002, no. 724, 2002.
[19] F. Ma, Y. Wang, Study on the extension of lean operation limit through hydrogen enrichment in a natural gas spark-ignition engine, Int. J. Hydrogen Energy 33 (4) (2008) 1416–1424.
[20] L.M. Das, R. Gulati, P.K. Gupta, Comparative evaluation of the performance characteristics of a spark ignition engine using hydrogen and compressed natural gas as alternative fuels, Int. J. Hydrogen Energy 25 (8) (2000) 783–793.
[21] M. Baratta, S. D'Ambrosio, and D. A. Misul, "Performance and Emissions of a Turbocharged Spark Ignition Engine Fuelled with CNG and CNG/Hydrogen Blends," SAE Technical Papers, vol. 2, 2013.
[22] M. Ilbas, A.P. Crayford, I. Yilmaz, P.J. Bowen, N. Syred, Laminar-burning velocities of hydrogen-air and hydrogen-methane-air mixtures: an experimental study, Int. J. Hydrogen Energy 31 (12) (2006) 1768–1779.
[23] M. Baratta, S. d'Ambrosio, D. Misul, E. Spessa, Effects of H 2 Addition to compressed natural gas blends on cycle-to-cycle and cylinder-to-cylinder combustion variation in a spark-ignition engine, J. Eng. Gas Turbines Power 136 (5) (2013) 051502.
[24] D. Soleri, et al., Effects of methane/hydrogen blends on engine operation: experimental and numerical investigation of different combustion modes, SAE Int. J. Engines 3 (2) (2010) 223–243.
[25] J.B. Heywood, Internal Combustion Engine Fundamentals, Second ed., McGraw-Hill Education, 2018.
[26] S. Hann, M. Grill, M. Bargende, Laminar flame speed engine simulation of lean combustion and exhaust gas recirculation at high load, MTZ Worldw. 79 (4) (2018) 26–33.
[27] P. Dimopoulos, K. Boulouchos, C. Rechsteiner, P. Soltic, and R. Hotz, "Combustion Characteristics of Hydrogen-Natural Gas Mixtures in Passenger Car Engines," SAE Technical Paper, vol. 2007-Septe, 2007.
[28] M. Kaiadi, P. Tunestål, B. Johansson, How hythane with 25% hydrogen can affect the combustion in a 6-cylinder natural-gas engine, SAE Int. J. Fuels Lubr. 3 (2) (2010) 47–59.
[29] V. Knop, A. Benkenida, S. Jay, O. Colin, Modelling of combustion and nitrogen oxide formation in hydrogen-fuelled internal combustion engines within a 3D CFD code, Int. J. Hydrogen Energy 33 (19) (2008) 5083–5097.
[30] G.M. Kosmadakis, D.C. Rakopoulos, C.D. Rakopoulos, Methane/hydrogen fueling a spark-ignition engine for studying NO, CO and HC emissions with a research CFD code, Fuel 185 (2016) 903–915.
[31] C.D. Rakopoulos, G.M. Kosmadakis, E.G. Pariotis, Evaluation of a combustion model for the simulation of hydrogen spark-ignition engines using a CFD code, Int. J. Hydrogen Energy 35 (22) (2010) 12545–12560.
[32] O. Colin, A. Benkenida, The 3-zones Extended Coherent Flame Model (ECFM3Z) for computing premixed/diffusion combustion, Oil Gas Sci. Technol. 59 (6) (2004) 593–609.
[33] C.W. Zhou, et al., An experimental and chemical kinetic modeling study of 1,3-butadiene combustion: Ignition delay time and laminar flame speed measurements, Combust. Flame 197 (2018) 423–438.
[34] H. El Merhubi, A. Kéromnès, G. Catalano, B. Lefort, L. Le Moyne, A high pressure experimental and numerical study of methane ignition, Fuel 177 (2016) 164–172.
[35] C. Ji, D. Wang, J. Yang, S. Wang, A comprehensive study of light hydrocarbon mechanisms performance in predicting methane/hydrogen/air laminar burning velocities, Int. J. Hydrogen Energy 42 (27) (2017) 17260–17274.
[36] E.J.K. Nilsson, A. van Sprang, J. Larfeldt, A.A. Konnov, The comparative and combined effects of hydrogen addition on the laminar burning velocities of methane and its blends with ethane and propane, Fuel 189 (2017) 369–376.
[37] V. S. I. D. T. of M. and H. H. D. in C. D. J. Shao, D.F. Davidson, R.K. Hanson, B. Samuel, S. Vasu, Ignition delay times of methane and hydrogen highly diluted in carbon dioxide, in: A. Sasoh, T. Aoki, M. Katayama (Eds.), Proceedings of the 31st International Symposium on Shock Waves 1, ISSW 2017, Cham, Springer, 2019.
[38] O. Pryor, et al., High pressure shock tube ignition delay time measurements during oxy-methane combustion with high levels of CO2 dilution, J. Energy Resour. Technol. 139 (4) (2017) 042208/1-6.
[39] N. Donohoe, et al., Ignition delay times, laminar flame speeds, and mechanism validation for natural gas/hydrogen blends at elevated pressures, Combust. Flame 161 (6) (2014) 1432–1443.
[40] J. Huang, P.G. Hill, W.K. Bushe, S.R. Munshi, Shock-tube study of methane ignition under engine-relevant conditions: experiments and modeling, Combust. Flame 136 (1-2) (2004) 25–42.
[41] F. Arpaia, "Laminar flame speed prediction for natural gas/hydrogen blends and application to the combustion modeling in IC Engines," 2019.
[42] M. Metghalchi, J.C. Keck, Burning velocities of mixtures of air with methanol, isooctane, and indolene at high pressure and temperature, Combust. Flame 48 (C) (1982) 191–210.
[43] Ö. L. Gülder, "Correlations of Laminar Combustion Data for Alternative s.i. Engine Fuels," in SAE Technical Papers, 1984.
[44] M. Baratta et al., "Experimental and Numerical Analysis of Diluted Combustion in a Direct Injection CNG Engine Featuring Post- Euro-VI Fuel Consumption Targets," SAE Technical Papers, vol. 1, 2018.
[45] R. Scarcelli, J. Sevik, T. Wallner, K. Richards, E. Pomraning, P.K. Senecal, Capturing cyclic variability in egr dilute si combustion using multi-cycle rans, in: Proceedings of the ASME 2015 Internal Combustion Engine Division Fall Technical Conference, ICEF, 2, 2015, pp. 1–11. 2015.
[46] L. Vervisch, D. Veynante, Turbulent combustion modeling, Prog. Energy Combust. Sci. 28 (3) (2002) 193–266.
[47] H.K. Versteeg, W.M. Malalasekera, Introduction to Computational Fluid Dynamics, M, Second ed., Pearson Prinston Hall, 2016.
[48] J. Göttgens, F. Mauss, N. Peters, Analytic approximations of burning velocities and flame thicknesses of lean hydrogen, methane, ethylene, ethane, acetylene, and propane flames, Symp. Combust. 24 (1) (1992) 129–135.
[49] R. Blint, The relationship of the laminar flame width to flame speed, Combust. Sci. Technol. 49 (1–2) (1986) 79–92.
[50] F. Li, Z. Wang, Y. Wang, B. Wang, High-efficiency and clean combustion natural gas engines for vehicles, Autom. Innov. 2 (4) (2019) 284–304.
[51] M. Baratta et al., "Experimental and Numerical Analysis of Diluted Combustion in a Direct Injection CNG Engine Featuring Post- Euro-VI Fuel Consumption Targets," SAE Technical Papers, vol. 2018-April, 2018.
[52] W. Li, Z. Liu, Z. Wang, Y. Xu, Experimental investigation of the thermal and diluent effects of EGR components on combustion and NOx emissions of a turbocharged natural gas SI engine, Energy Convers. Manag. 88 (2014) 1041–1050.
[53] J. Wang, F. Matsuno, M. Okuyama, Y. Ogami, H. Kobayashi, Z. Huang, Flame front characteristics of turbulent premixed flames diluted with CO2 and H2O at high pressure and high temperature, Proc. Combust. Inst. 34 (1) (2013) 1429–1436.
[54] F. Halter, C. Chauveau, I. Gökalp, Characterization of the effects of hydrogen addition in premixed methane/air flames, Int. J. Hydrogen Energy 32 (13) (2007) 2585–2592.